



**HAL**  
open science

## Lidar-relevant radiative properties of soot fractal aggregate ensembles

Lucas Paulien, Romain Ceolato, Laurent Soucasse, Franck Enguehard,  
Anouar Soufiani

► **To cite this version:**

Lucas Paulien, Romain Ceolato, Laurent Soucasse, Franck Enguehard, Anouar Soufiani. Lidar-relevant radiative properties of soot fractal aggregate ensembles. *Journal of Quantitative Spectroscopy and Radiative Transfer*, 2020, 241, pp.106706. 10.1016/j.jqsrt.2019.106706 . hal-02349170

**HAL Id: hal-02349170**

**<https://hal.science/hal-02349170v1>**

Submitted on 14 Feb 2020

**HAL** is a multi-disciplinary open access archive for the deposit and dissemination of scientific research documents, whether they are published or not. The documents may come from teaching and research institutions in France or abroad, or from public or private research centers.

L'archive ouverte pluridisciplinaire **HAL**, est destinée au dépôt et à la diffusion de documents scientifiques de niveau recherche, publiés ou non, émanant des établissements d'enseignement et de recherche français ou étrangers, des laboratoires publics ou privés.

# Lidar-relevant radiative properties of soot fractal aggregate ensembles

Lucas Paulien<sup>a,b</sup>, Romain Ceolato<sup>a,\*</sup>, Laurent Soucasse<sup>b</sup>, Franck Enguehard<sup>c</sup>, Anouar Soufiani<sup>b</sup>

<sup>a</sup>ONERA, The French Aerospace Lab, Université de Toulouse, FR 31055, France

<sup>b</sup>Laboratoire EM2C, CentraleSupélec, Université Paris-Saclay, Gif-sur-Yvette, 91192, France

<sup>c</sup>Institut PPrime, CNRS, Université de Poitiers, ISAE-ENSMA, 86962, Futuroscope, Chasseneuil, France

---

## Abstract

This study presents the averaged lidar-relevant radiative properties of numerically generated soot fractal aggregate ensembles. The radiative properties of these aggregates have been computed using the Superposition T-Matrix Method, with emphasis put on those that are most relevant to lidar application; the backscattering and extinction cross-sections, the Lidar Ratio and the Linear Depolarization Ratio. These lidar-relevant radiative properties have been computed over a broad spectrum, going from the ultraviolet to the near infrared, in order to address lidar instrument need for *a priori* knowledge in signal inversion procedures and measurement analysis. By averaging the computed radiative properties according to each set of morphological parameters, we obtain statistically representative results and we study the impacts of morphological changes on these lidar-relevant radiative properties. Our results show a strong impact of the primary particle radius on all considered radiative properties, while the number of primary particles induce significant variations on the cross-sections only. The fractal dimension, although being an essential morphological parameter, has a weak influences on the lidar-relevant radiative properties.

*Keywords:* Soot Fractal Aggregates, lidar, Aerosol radiative properties, Modelling, T-Matrix

---

\*Corresponding author : romain.ceolato@onera.fr

## 1. Introduction

Soot particles are fine matter aerosols emitted from both natural and anthropogenic combustion processes, such as biomass burning or aeronautical engines. Freshly emitted soot particles are composed of clustered spherical primary particles, called monomers, which are formed during the incomplete combustion of organic materials. The structures resulting from the aggregation of primary particles are complex, and are often referred to as fractal-like shape [1, 2]. The molecular composition as well as the sub-micronic size of these particles are problematic for human health, being cause of lung and artery diseases or cancers [3]. Moreover these particles can act as cloud condensation nuclei leading to the formation of condensation trails along plane tracks at high altitude [4]. Soot particles are also characterised by their high imaginary part of the optical index, therefore having a strong ability to absorb light in a wide spectrum.

These properties influence global climate by increasing the radiative forcing with both direct and indirect effects [5, 6]. Both impacts on air quality and climate of soot particles are related to their morphology [3, 7]. Indeed, these Soot Fractal Aggregates (SFA) present various sizes and shapes according to the process of combustion that has led to their formation [8]. The characterisation of the morphological properties of emitted SFAs is therefore needed to evaluate and study the effect of these particles on climate and health. Several instrumental techniques are used to study these aggregates. *Ex situ* techniques such as electron microscopy can be used in order to precisely characterise the morphology of soot emitted from flames [9], but this method requires sampling procedures which can produce morphological changes and also requires extensive use in order to obtain statistically representative results. *In situ* techniques have the advantage of being non-intrusive, eliminating the possible bias induced by sampling. For example, X-ray Photoelectron Spectroscopy and Near Edge X-Ray Absorption Fine Structure have been used in order to study the composition and oxidation properties of airborne soot [10]. Another method is the Laser Induced Incandescence technique, which can be used to retrieve the soot volume fraction or the soot mass concentration profiles [11], or to determine the primary particle size [12]. Angular light scattering measurements are also able to measure the size distribution of SFAs [13].

To our knowledge, one limitation of these *in situ* instrumental techniques is their current inapplicability to study soot particles in atmospheric envi-

38 ronment while keeping their non-intrusive aspect. To study soot particles in  
39 atmospheric conditions, remote sensing techniques are especially of interest.  
40 Light Detection And Ranging (lidar) instruments rely on the collection and  
41 detection of the light backscattered by the particles and molecules inside the  
42 volume of an emitted laser pulse in order to study this interacting medium.  
43 The detection of this backscattered light and the analysis of the associated  
44 signal can provide information on the particles, such as their concentration,  
45 size distribution or morphological properties [14, 15]. These systems have  
46 already proven their ability to characterise and qualify different types of  
47 aerosols [16, 17] from remote area.

48 Because of the underdetermination of the problem associated with lidar  
49 measurements, the processing of the signals provided by these instruments  
50 relies on *a priori* knowledge of the radiative properties of the medium under  
51 study. This has led to the measurement and modelling of different types of  
52 airborne particle radiative properties with procedures that are in need of con-  
53 tinuous improvement. The backscattering and extinction cross-sections, the  
54 Linear Depolarization Ratio (LDR) as well as the Lidar Ratio (LR) are espe-  
55 cially useful to process and analyse lidar measurements. The backscattering  
56 and extinction cross-sections are directly involved in the inversion methods  
57 allowing to retrieve an aerosol concentration, while the LDR is often used  
58 as a discriminating parameter in order to characterise the airborne particle  
59 type. The Lidar Ratio is also a crucial parameter in the inversion algorithms  
60 of lidar signals [18].

61 The main objectives of this study are to quantify these radiative prop-  
62 erties for statistically representative ensembles of SFAs and to study the  
63 effects induced by morphological changes. In this sense, we are interested in  
64 the light-matter interaction processes, in the framework of lidar application.  
65 After introducing this framework, we describe the models used to numerically  
66 generate SFAs and to calculate their radiative properties. Following the frac-  
67 tal model, SFAs are generated with a variety of morphological parameters.  
68 Statistically representative ensembles of SFAs are generated in order to eval-  
69 uate the standard deviation of our results. Using the Multi-Sphere T-Matrix  
70 code [19], we chose to compute these lidar-relevant radiative properties from  
71 300 to 1100 nm, allowing to address a wide range of lidar instruments. After  
72 presenting our results, we discuss the impacts of the morphological param-  
73 eters on these properties.

74 **2. Lidar framework**

Polarization-resolved lidar are instruments able to measure simultaneously several states of polarization of the received backscattered light. The most common type of polarization-resolved lidar instruments can record the co-polarized ( $\parallel$ ) and cross-polarized ( $\perp$ ) components of the backscattered light relative to the emitted beam polarization plane. The elastic lidar equation under the single-scattering approximation provides the range-resolved backscattered power  $P(r)$  at a given range  $r$  from the receiver as:

$$P_{\parallel,\perp}(r, \lambda) = K_{\parallel,\perp}(r, \lambda)O(r, \lambda)U_{\parallel,\perp}(r, \lambda) \quad (1)$$

where the  $\parallel, \perp$  subscripts refers to the state of polarization of the received light relative to the emitted pulse,  $K(r, \lambda)$  is the lidar instrument function and  $O(r, \lambda)$  is the range-dependent overlap function.  $U(r, \lambda)$  is the attenuated backscattering function defined as :

$$U_{\parallel,\perp}(r, \lambda) = \beta_{\parallel,\perp}(r, \lambda) \exp\left(-2 \int_0^r \alpha(r', \lambda) dr'\right) \quad (2)$$

75 where  $\beta(r, \lambda)$  and  $\alpha(r, \lambda)$  are the backscattering and extinction coefficients,  
76 also referred to as lidar products, respectively defined as:

$$\begin{aligned} \beta_{\parallel,\perp}(r, \lambda) &= \sum_{i=m,p} \beta_{\parallel,\perp,i}(r, \lambda) \\ \beta_{\parallel,\perp,p}(r, \lambda) &= \int_0^{A_{max}} n_p(a, r) C_{back,\parallel,\perp}(a, \lambda) da \end{aligned} \quad (3)$$

77

$$\begin{aligned} \alpha(r, \lambda) &= \sum_{i=m,p} \alpha_i(r, \lambda) \\ \alpha_p(r, \lambda) &= \int_0^{A_{max}} n_p(a, r) C_{ext}(a, \lambda) da \end{aligned} \quad (4)$$

78 The subscripts  $m$  and  $p$  refer respectively to the molecular and particular  
79 contributions,  $a$  is a characteristic length of the particles ranging from 0  
80 to  $A_{max}$ , and  $n_p$  is the particle size distribution. The quantities  $C_{back}$  and  
81  $C_{ext}$  are the wavelength and size dependent backscattering and extinction  
82 cross-sections respectively, and are specific to the type, size, morphology and  
83 complex optical index of the particles.

84 In the case of SFAs being present in the scattering volume, Equations  
 85 (3) and (4) are hardly applicable. Indeed, SFAs are non-spherical and highly  
 86 irregularly shaped particles, so that the definition of a characteristic length  $a$   
 87 is a complex endeavour [20]. In the simplest case, if we consider a scattering  
 88 volume containing exclusively a monodisperse distribution of SFAs, meaning  
 89 that all particles have exactly the same morphology, the integral formulation  
 90 of the particular backscattering and extinction coefficients in Equations (3)  
 91 and (4) can be reformulated as :

$$\beta_{\parallel,\perp,mono}(r, \lambda) = \frac{3f_v(r)}{4\pi N_m r_m^3} C_{back,\parallel,\perp}(r_m, N_m, \lambda) \quad (5)$$

$$\alpha_{mono}(r, \lambda) = \frac{3f_v(r)}{4\pi N_m r_m^3} C_{ext}(r_m, N_m, \lambda) \quad (6)$$

92  
 93 where  $f_v$  is the soot volume fraction and  $r_m$  and  $N_m$  are the monomer ra-  
 94 dius and number of monomers per aggregate respectively. The soot volume  
 95 fraction  $f_v$  is defined as :

$$f_v = N \frac{4}{3} \pi N_m r_m^3 \quad (7)$$

96 where  $N$  is the number density of aggregates.

97 The cross-sections in Equations (5) and (6) might nevertheless also de-  
 98 pend on other parameters, such as the fractal dimension which will be defined  
 99 in Section 3.1 or any other *ad hoc* parameter describing the morphology of  
 100 SFAs. The dependence of the cross-sections on these parameters will be im-  
 101 plicitely assumed in the rest of this section in order to lighten the notations

102 The ratio of the cross-polarized and co-polarized signals gives the volume  
 103 depolarization ratio :

$$\delta_v(r, \lambda) = \frac{K_{\perp}(r, \lambda) \beta_{\perp}(r, \lambda)}{K_{\parallel}(r, \lambda) \beta_{\parallel}(r, \lambda)} \quad (8)$$

104 Equations (3) to (6) link the retrievable lidar products to the radiative  
 105 properties of individual particles. In order to process these lidar products,  
 106 *a priori* knowledge on the particle radiative properties is necessary, as, in  
 107 the general case, neither the size distribution (volume fraction in case of  
 108 monodisperse SFAs) or morphology are known.

109 Considering randomly oriented particles, the scattering properties in the  
 110 backward direction of these particles are expressed using the random orien-  
 111 tation scattering matrix [21, 22]. In the backward direction, this matrix is  
 112 diagonal :

$$\mathbf{F}(\theta = \pi, \lambda) = \begin{pmatrix} F_{11}(\pi, \lambda) & 0 & 0 & 0 \\ 0 & F_{22}(\pi, \lambda) & 0 & 0 \\ 0 & 0 & F_{33}(\pi, \lambda) & 0 \\ 0 & 0 & 0 & F_{44}(\pi, \lambda) \end{pmatrix} \quad (9)$$

113 This matrix provides the description of the backscattered light from the  
 114 corresponding particles. Using this matrix, radiative properties convenient  
 115 to lidar application are constructed, namely the unpolarized backscattering  
 116 cross-section  $C_{back}$ , the Lidar Ratio (LR) and the Linear Depolarization Ratio  
 117 (LDR)  $\delta$ . Hereafter, we use the generic term lidar cross-sections to refer to  
 118 the backscattering and extinction cross-sections, while the LR and LDR are  
 119 named as lidar parameters, being ratios of cross-sections.

120 Considering a scattering medium with negligible molecular contribution  
 121 ( $\beta_{\parallel, \perp, m} \ll \beta_{\parallel, \perp, p}$  and  $\alpha_m \ll \alpha_p$ ), these lidar-relevant radiative properties  
 122 are expressed as :

$$C_{back}(\lambda) = \frac{\lambda^2}{4\pi^2} F_{11}(\pi, \lambda) = C_{back, \parallel}(\lambda) + C_{back, \perp}(\lambda) \quad (10)$$

$$LR(\lambda) = \frac{C_{ext}(\lambda)}{C_{back}(\lambda)} \quad (11)$$

$$\delta(\lambda) = \frac{C_{back, \perp}(\lambda)}{C_{back, \parallel}(\lambda)} = \frac{F_{11}(\pi, \lambda) - F_{22}(\pi, \lambda)}{F_{11}(\pi, \lambda) + F_{22}(\pi, \lambda)} \propto \delta_v \quad (12)$$

125 The expressions of these lidar-relevant radiative properties in Equations  
 126 (10), (11) and (12) are directly useful in the exploitation of the lidar products  
 127 according to Equations (3) and (4).

128 The Lidar Ratio (LR) is a lidar parameter which quantifies the ratio  
 129 of the extinguished light relatively to the backscattered light. It is a con-  
 130 venient parameter to express the potential backscattered signal obtained  
 131 by a lidar instrument, and is often used in lidar signal inversion methods  
 132 such as the Klett-Fernald's algorithm [18]. The Linear Depolarization Ra-  
 133 tio (LDR) is often used in lidar applications as a discriminating parameter

134 in order to classify the particles inside the measurement volume. This li-  
 135 dar parameter strongly depends on the morphology of the scatterer. Indeed,  
 136 spherical particles scattering matrix elements are simplified by the relation-  
 137 ship  $F_{11}(\pi) = F_{22}(\pi)$ . According to Equation (12), this relationship directly  
 138 results in a null LDR for spherical particle. Hence, the LDR provides in-  
 139 formation on the non-sphericity of a particle. In lidar application, it can  
 140 be compared to the volume LDR ( $\delta_v$ ) to qualitatively specify which type of  
 141 particles is present in the scattering volume.

### 142 3. Methodology

#### 143 3.1. Generation of soot fractal aggregates ensembles

144 Soot aggregates are highly irregularly-shaped particles which are com-  
 145 posed of clustered spherical primary particles, also called monomers. These  
 146 particles are to be distinguished from black carbon particles, which refers to  
 147 any particle with a high light absorption capacity and a high carbon con-  
 148 tent [23]. In this article, we focus on freshly emitted soot aggregates. These  
 149 particles can be described using the fractal concept Forrest and Witten Jr  
 150 [1] which provides a convenient formulation of their morphologies. In this  
 151 model, the number of monomers is linked to the overall size of the aggregate  
 152 with the power-law :

$$N_m = k_f \left( \frac{R_g}{r_m} \right)^{D_f} \quad (13)$$

153 where  $N_m$  is the number of monomers,  $r_m$  is the monomer radius,  $R_g$  is the  
 154 radius of gyration,  $k_f$  is the fractal prefactor and  $D_f$  is the fractal dimension.  
 155 The radius of gyration  $R_g$  is a quantity that represents the overall radius of  
 156 an aggregate and is defined as :

$$R_g = \sqrt{\frac{1}{N_m} \sum_{i=1}^{i=N_m} x_i^2} \quad (14)$$

157 where  $x_i$  is the distance from the  $i^{\text{th}}$  monomer center to the center of mass of  
 158 the aggregate. The fractal prefactor  $k_f$  is thought to be related to the local  
 159 packing of the monomers [24, 25]. The fractal dimension  $D_f$  is a parame-  
 160 ter the value of which lies between 1 and 3 and which provides information  
 161 on the overall morphology of an aggregate. Indeed, as the fractal dimen-  
 162 sion decreases, the corresponding aggregate presents a more and more linear



163 structure, while a compact aggregate is described by a fractal dimension  
164 approaching 3.

165 Various values of the monomer radius have been reported in the literature,  
166 ranging from 10 – 25 nm [26, 27] up to 40 – 50 nm mean radius in large  
167 pool fires [28, 29]. The reported values of the fractal dimension and fractal  
168 prefactor are also variable, the former being usually comprised between  $D_f =$   
169 1.6 and  $D_f = 2.0$  [30], but they are predominantly found to be close to  
170  $D_f \approx 1.8$  with a fractal prefactor of  $k_f \approx 1.3$  [31].

171 The fractal aggregates used in this study have been generated using  
172 the tunable Cluster-Cluster aggregation algorithm developed by Mackowski  
173 [32, 33]. This algorithm allows the generation of the monomer positions for  
174 an aggregate while fixing the values of the fractal parameters  $k_f$  and  $D_f$ ,  
175 as well as the number of monomers  $N_m$ . Twenty-seven ensembles of one  
176 hundred SFAs have been generated using this algorithm, with the fractal  
177 prefactor always set to  $k_f = 1.3$  and the number of monomers to  $N_m = 45,$   
178 125 or 450. The fractal dimension has been set to either  $D_f = 1.6, 1.8$  or  
179 2.0 and the monomer radius to  $r_m = 10$  nm, 20 nm or 40 nm. Examples of  
180 generated aggregates are shown in Figure 1. Using Equation (14), we calcu-  
181 lated the radius of gyration of each aggregate. When averaging these radii  
182 over ensembles of same morphological parameters, we found less than 0.3%  
183 deviation from the mean value of the radius of gyration. The average results  
184 are represented by the markers on Figure 1.

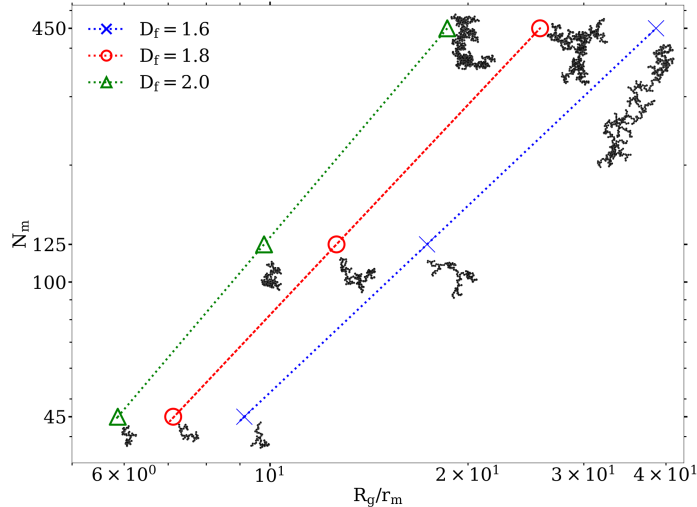


Figure 1: Number of monomers against the radius of gyration normalized by the monomer radius for ensembles of fractal dimension  $D_f = 1.6$ ,  $1.8$ , and  $2.0$ . Each marker represents one of the generated aggregate ensembles and the dashed lines are the fitted curves using equation 13. The fitting parameters are  $D_f = 1.5975 \pm 0.0002$  and  $k_f = 1.3127 \pm 0.0009$  (blue curve, cross),  $D_f = 1.7968 \pm 0.0002$  and  $k_f = 1.3141 \pm 0.0010$  (red curve, circles),  $D_f = 1.9965 \pm 0.0002$  and  $k_f = 1.3142 \pm 0.0008$  (green curve, triangles). Examples of the aggregate morphologies are represented nearby the corresponding markers. In these representations, the monomer radius is set to the same arbitrary value, and the aggregates have been orientated so that the longest vector linking any couple of monomer centers is placed in the plane of the figure.

185 The fractal parameters  $D_f$  and  $k_f$  of each ensemble have been retrieved by  
 186 fitting the number of monomers against the radius of gyration normalized by  
 187 the monomer radius using Equation (13). The relative discrepancy between  
 188 initial and retrieved values of the fractal parameters are less than 1.5%, hence  
 189 being in very good agreement as shown in Figure 1. Hereafter, the initial  
 190 values are used in order to lighten the notations.

191 Although the aggregates of each ensemble can be characterised by the  
 192 same morphological parameters, each aggregate still presents its own disposi-  
 193 tion of the monomers in space. These different morphologies within the same  
 194 ensemble can result in variations of the radiative properties. Indeed, previous  
 195 studies have highlighted the importance of using ensemble averaging as well  
 196 as orientation averaging [34]. In our study we compute random-orientation  
 197 radiative properties, and then we average these properties over the one hun-  
 198 dred aggregates of each ensemble. Results (not presented in this paper)

199 show that as we increase the number of aggregates in the ensembles from  
 200 one to around fifty, there can be strong variations of the standard deviation  
 201 at certain wavelengths. By adding more aggregates into the ensembles, these  
 202 variations attenuate. We chose to use ensembles of one hundred aggregates  
 203 as a compromise between representativity of the aggregate morphologies and  
 204 their associated radiative property standard deviation, and the computation  
 205 time and resources.

### 206 3.2. Refractive index of soot particles

207 The computation of the radiative properties also requires the material  
 208 complex optical index. Variable values of the real and imaginary parts of  
 209 the refractive index of soot particles have been reported in the literature,  
 210 under different conditions of emission, soot temperature, fuel, wavelength and  
 211 determination method [35, 36, 37]. As our intent is to provide representative  
 212 values of the lidar-relevant radiative properties on a large spectrum ( $300 \text{ nm} \leq$   
 213  $\lambda \leq 1100 \text{ nm}$ , with a wavelength step  $\Delta\lambda = 20 \text{ nm}$ ), we used the wavelength-  
 214 dependent dispersion law from Chang and Charalampopoulos [38], as shown  
 215 in Figure 2.

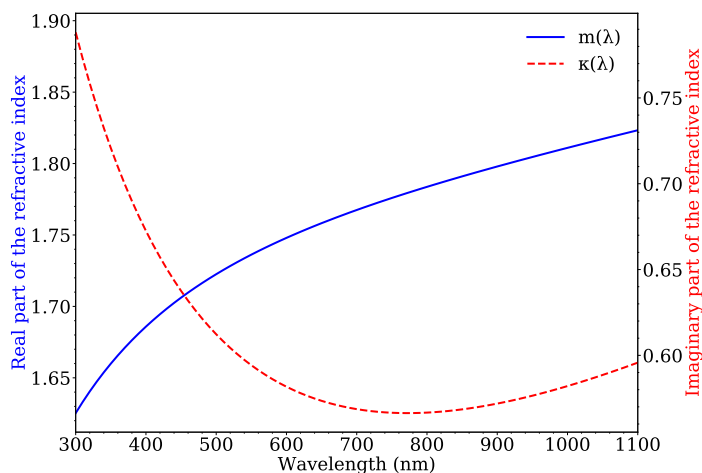


Figure 2: Refractive index  $m(\lambda) = n(\lambda) + i\kappa(\lambda)$  used in this study [38].

### 216 3.3. Modelling of the lidar-relevant radiative properties

217 Different methods can be used to model the radiative properties of SFAs.  
 218 The well known Lorenz-Mie theory can be used to calculate the radiative

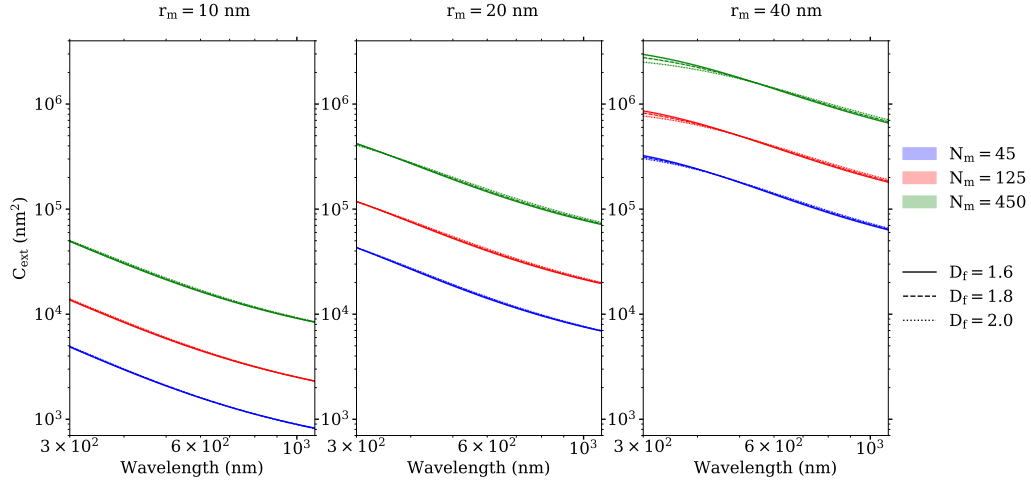
219 properties of spheres [39], but this method has shown poor accuracy when  
220 applied to SFAs because of the use of non-representative equivalent spheres  
221 [20, 40]. The Rayleigh-Debye-Gans for Fractal Aggregates (RDG-FA) theory  
222 is another method which is specifically designed to compute the radiative  
223 properties of fractal aggregates [41]. This approximation provides good an-  
224 gles integrated results, *e.g.* the extinction cross-sections. However, the angle  
225 dependent results obtained using RDG-FA such as the scattering matrix ele-  
226 ments can be inaccurate, especially for high primary particle size parameter  
227 [42]. The Discrete Dipole Approximation method has also been used on  
228 realistic aggregate morphologies [43, 44, 45]. This method provides quan-  
229 tification of the scattered field from a particle of any shape illuminated by  
230 any incoming field. The limitation of this method comes from its computa-  
231 tionally intensive character, especially if orientation averaged and ensemble  
232 averaged results are sought. The Superposition T-Matrix (STM) method is  
233 commonly used for the computation of SFA radiative properties [46, 47]. This  
234 method also shows limitations, as the scatterer must be composed of strictly  
235 non-overlapping spheres, preventing the computation of complex morpho-  
236 logical properties such as sphere overlapping, necking or complex coating  
237 phenomenon. This applicability criterion is met by the fractal aggregate  
238 model described in Section 3.1.

239 The STM method consists in expressing the scattered field by the overall  
240 aggregate as the superposition of the partial fields contributed by each indi-  
241 vidual sphere, taking into account the internal multiple scattering between  
242 spheres. As a detailed description of this method and of the mathematics  
243 involved is available in the papers from Mackowski and Mishchenko [48], we  
244 only provide a short description of the principles of this method hereafter.  
245 The external incoming field and outgoing field of each sphere are expanded  
246 into Vector Spherical Wave Functions centered about the sphere origins, and  
247 the associated expansion coefficients are calculated. The transition matrix  
248 (T-Matrix) transforms the outgoing field centered about one sphere origin  
249 into the incoming field of another sphere. This allows the computation of  
250 the internal multiple scattering among monomers, *i.e.* the way the scattered  
251 field from one sphere impacts the others. The sets of equations involved are  
252 iteratively solved until a specified convergence criterion is met regarding the  
253 radiative properties of each sphere, and the sphere-centered T-matrices are  
254 then transformed into a single cluster-centered T-matrix. This T-matrix al-  
255 lows the computation of the coefficients of the far-field scattered transverse  
256 spherical wave, which in turn leads to the computation of the amplitude

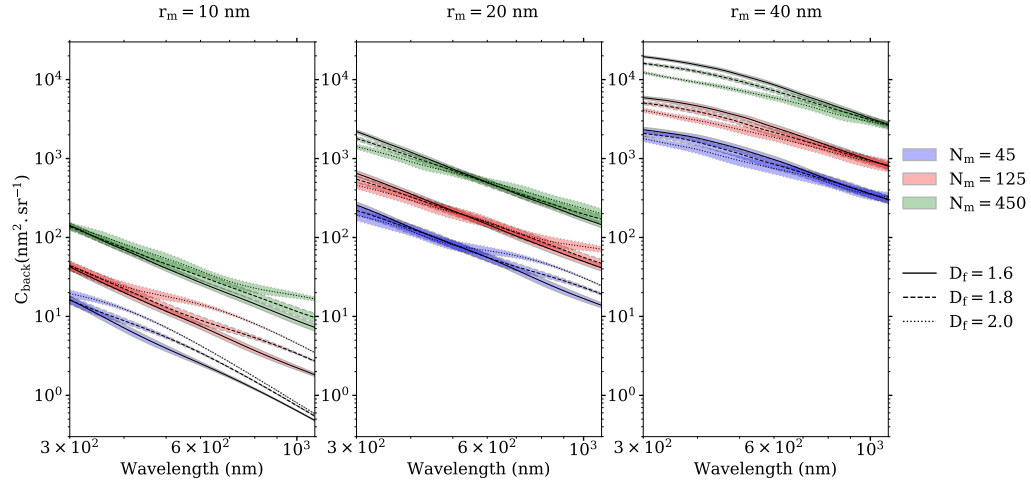
257 scattering matrix. By applying the linearized form of the two sets of rota-  
258 tion functions to (i) first the T-Matrix to compute the scattering coefficients;  
259 (ii) second the amplitude scattering matrix to compute the orientation aver-  
260 aged amplitude scattering matrix, simplification of the random orientation  
261 scattering matrix calculation is achieved. The random orientation extinction  
262 cross-section is also calculated from the cluster-centered T-Matrix. In our  
263 study, we used the Multi-Sphere T-Matrix (MSTM) code [19].

#### 264 **4. Numerical results**

265 Using the MSTM code, each individual SFA's lidar-relevant radiative  
266 properties have been calculated. Afterwards, the SFA's radiative proper-  
267 ties have been averaged over their corresponding morphological ensemble  
268 with the same number of monomers  $N_m$ , monomer radius  $r_m$  and fractal  
269 dimension  $D_f$ .



(a) Extinction cross-sections.



(b) Backscattering cross-sections.

Figure 3: Extinction (a) and backscattering (b) cross-sections of SFA ensembles. The three panels are ordered according to the SFA ensemble monomer radius, *i.e.* 10 nm, 20 nm, and 40 nm monomer radius from left to right. The blue, red and green curves are associated with aggregates composed of 45, 125, and 450 monomers respectively. The coloured stripes represent the standard deviations to the mean values of the cross-sections. The solid, dashed, and dotted lines represent different values of the fractal dimension, *i.e.*  $D_f = 1.6$ ,  $D_f = 1.8$ , and  $D_f = 2.0$  respectively. The fractal prefactor of all aggregates is set to  $k_f = 1.3$ .

271 According to Figure 3a, the extinction cross-sections present a consistent  
272 spectral and morphological dependence across all ensembles. The extinction  
273 cross-sections are decreasing with wavelength, and increasing with monomer  
274 radius. Higher number of monomers also results in higher cross-sections.  
275 Fractal dimension variations produce a negligible effect on the extinction  
276 cross-section, with the exception of the largest aggregate ensembles (*i.e.*  
277  $r_m = 40$  nm,  $N_m = 450$ ). In these cases, higher fractal dimensions result  
278 in lower extinction cross-sections in the UV part of the spectrum. The stan-  
279 dard deviations of the extinction cross-sections across all wavelength and  
280 ensembles are below 0.1%.

281 As shown in Figure 3b, the backscattering cross-sections are also decreas-  
282 ing with wavelength, with a standard deviation of about 10% over the whole  
283 spectrum for each ensemble of aggregates. A difference up to more than  
284 one order of magnitude between the backscattering cross-sections in the UV  
285 and in the NIR can be observed. This decrease with wavelength is more  
286 important for smaller aggregates, *i.e.* as the monomers are few and small.  
287 Comparing the Figures 3a and 3b, it is apparent that the backscattering  
288 cross-sections are decreasing more rapidly with wavelength than the extinc-  
289 tion cross-sections.

290 For the same other morphological parameters, doubling the monomer  
291 radius leads to a backscattering cross-section increase by a factor ranging  
292 from 10 in the UV part of the spectrum up to 50 in the NIR part. The  
293 backscattering cross-section decrease with wavelength is greater for smaller  
294 monomer radius. Hence, the monomer radius of the aggregates also influences  
295 the wavelength dependence of the radiative properties.

296 Increasing tenfold the number of monomers induces a 6 to 12 times in-  
297 crease of the backscattering cross-section when the monomer radius is equal  
298 to either  $r_m = 20$  nm or  $r_m = 40$  nm. For monomer radius  $r_m = 10$  nm,  
299 this factor ranges from 7 to 29. This difference for smaller monomers is  
300 most certainly due to the different spectral dependence of the backscatter-  
301 ing cross-sections. Indeed, the wavelength dependence of the backscattering  
302 cross-sections is also influenced by the number of monomers, with lower num-  
303 ber of monomers inducing a steeper decrease. The 10 nm radius ensembles  
304 in particular present the strongest variation.

305 The impact of the fractal dimension on the backscattering cross-section  
306 is interdependent on the monomer radius and number. Indeed, for small  
307 monomer radius as represented on the left panel of Figure 3b, the compact  
308 aggregates with higher fractal dimension present higher backscattering cross-

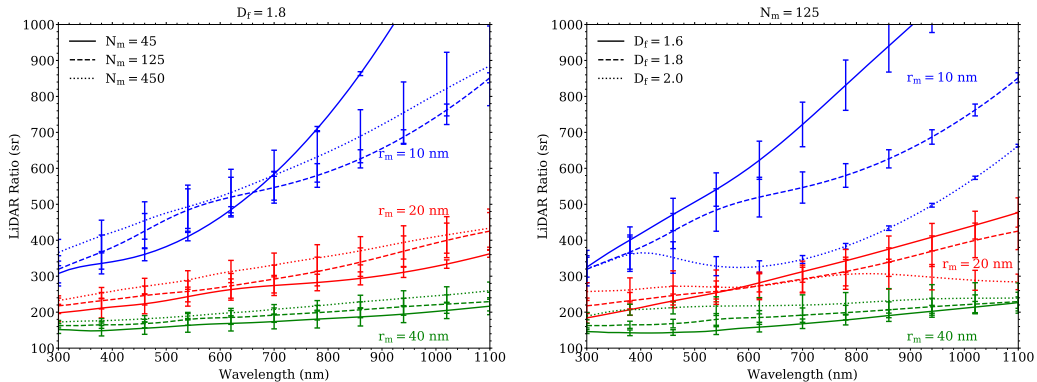
309 sections. In this panel, SFAs with few monomers, *i.e.*  $N_m = 45$ , present  
310 a noticeable separation of the curves for different fractal dimensions (blue  
311 curves) from the UV part to the NIR, while curves associated with higher  
312 numbers of monomers are separated at higher wavelengths. For  $r_m = 20$  nm,  
313 linear SFAs present higher backscattering cross-sections in the UV part of the  
314 spectrum, and conversely in the NIR part. SFA ensembles of  $r_m = 40$  nm  
315 monomer radius present increasingly ordered backscattering cross-sections  
316 with decreasing fractal dimension.

317 Some features of the different curves seem to be shifted at larger wave-  
318 lengths when increasing the overall size of the aggregates. For example, on  
319 the left panel of Figure 3b, the separation of the curves of different fractal  
320 dimensions occurs at larger wavelengths with higher monomer radius and/or  
321 number. The considered complex optical index varying only slightly in this  
322 spectrum, this indicates that a parameter similar to the usual size parameter  
323  $x = 2\pi a/\lambda$  could be driving the wavelength dependence of these radiative  
324 properties. However, the length scale involved still needs to be defined, and  
325 this study is out of the scope of this article.

#### 326 4.2. Lidar Ratio

327 As the LR is the ratio between the extinction cross-section and the  
328 backscattering cross-section, both morphological and spectral dependence of  
329 the LR are closely related to those of the lidar cross-sections. Indeed, Figure  
330 4 shows an increasing LR with larger wavelengths, which is consistent with  
331 the wavelength dependence of the lidar cross-sections.





(a) LR variation with monomer radius and number (b) LR variation with monomer radius and fractal dimension

Figure 4: LR of SFA ensembles. The three sets of coloured curves are ordered according to the SFA ensemble monomer radius, *i.e.* 10 nm, 20 nm, and 40 nm monomer radius for the blue, red and green curves respectively. The full, dashed and dotted lines are associated with aggregates composed of 45, 125, and 450 monomers respectively on Figure (a), and with  $D_f = 1.6, 1.8,$  and  $2.0$  on Figure (b). The error bars are plotted every four points and represent the standard deviations to the mean values of LRs. On Figure (a), the fractal dimension is set to  $D_f = 1.8$ , and on Figure (b) the number of monomers is set to  $N_m = 125$ . The fractal prefactor of all aggregates is set to  $k_f = 1.3$ .

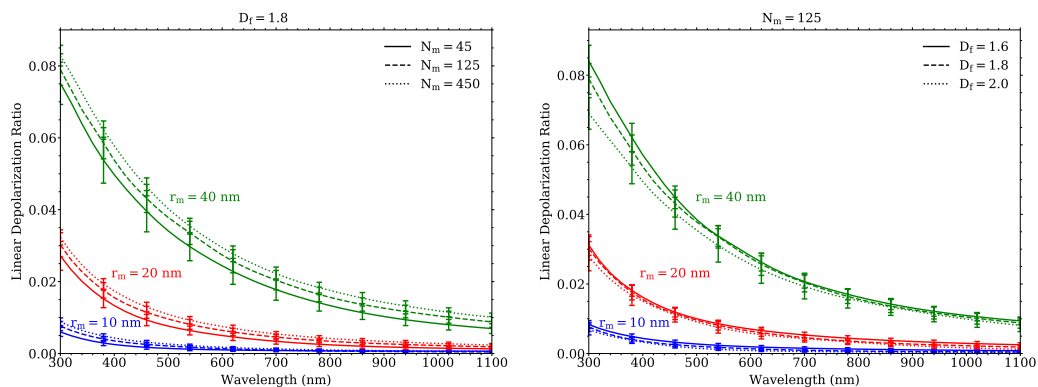
332 Similarly, larger monomer radius reduces the LR, which is consistent with  
 333 the increasing backscattering cross-section presented in Figure 3b. LR values  
 334 with different monomer radius show close values in the UV part of the spec-  
 335 trum, and diverge in the near infrared. Aggregates with smaller monomer ra-  
 336 dius present a more important increase of the LR. This relationship is also in  
 337 accordance with the spectral dependence of the backscattering cross-section  
 338 in Figure 3b.

339 Higher number of monomers also induces higher LR, with the noticeable  
 340 exception of the ensemble of smallest aggregates (*i.e.*  $r_m = 10$  nm,  $N_m =$   
 341 45). This ensemble wavelength dependence is most probably due to the  
 342 steeper decrease of the backscattering cross-section of this ensemble as shown  
 343 in Figure 3b (left panel; blue dashed line). The variation of the LR with  
 344 SFA's number of monomers is still small, the associated standard deviations  
 345 overlapping on many if not all parts of the spectrum.

346 Impacts of the fractal dimension are harder to evaluate, as several dis-  
 347 tinctive trends occur as a function of both wavelength and monomer radius.  
 348 Indeed, Figure 4b shows that for small aggregates (blue curves), a more

349 compact aggregate induces a lower LR, while large aggregates (green curves)  
 350 present the inverse feature. Intermediate size (red curves) presents both  
 351 trends, the former in the NIR part and the latter in the lower part of the  
 352 spectrum. Similarly, the standard deviations of the LRs are predominantly  
 353 affected by the backscattering cross-section standard deviations.

### 354 4.3. Linear Depolarization Ratio



(a) LDR variation with monomer radius and number (b) LDR variation with monomer radius and fractal dimension

Figure 5: LDRs of SFA ensembles. The blue, red and green colours are used to differentiate SFA ensembles of 10 nm, 20 nm, and 40 nm monomer radius respectively. The solid, dashed and dotted lines represent SFA ensembles of varying number of monomers and fractal dimension, *i.e.*  $N_m = 45$ ,  $N_m = 125$  and  $N_m = 450$ , respectively for Figure (a) in which case the fractal dimension is set to  $D_f = 1.8$ , and  $D_f = 1.6$ ,  $D_f = 1.8$ , and  $D_f = 2.0$  respectively for Figure (b) with the number of monomers set to  $N_m = 125$ . The fractal prefactor of all aggregates is set to  $k_f = 1.3$ .

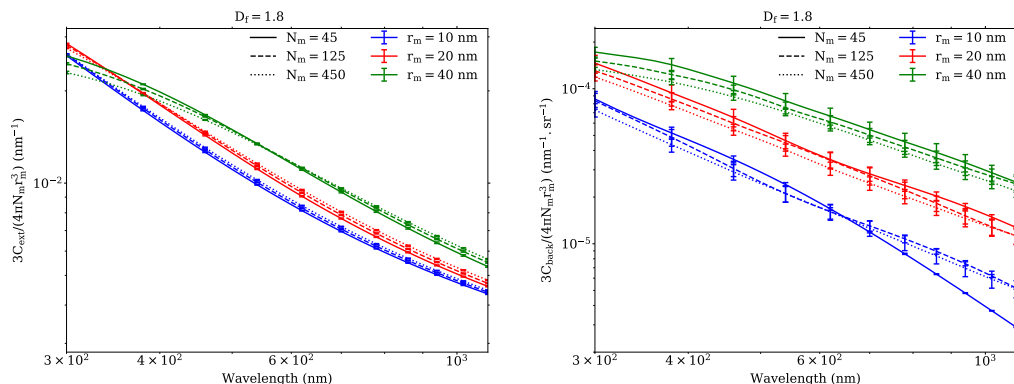
355 Figure 5 shows a decrease of the LDR and its associated standard deviation  
 356 with increasing wavelength. LDR variation with monomer radius is  
 357 similar to the backscattering cross-section dependence on  $r_m$ , with the LDR  
 358 increasing for larger monomer radius. For example, the LDR increases about  
 359 tenfold when the monomer radius passes from  $r_m = 10$  nm (Figure 5a; blue  
 360 curves) to  $r_m = 40$  nm (Figure 5a; green curves) at 300 nm wavelength. The  
 361 10 nm monomer radius LDRs are progressively reaching a near-zero thresh-  
 362 old as the wavelength increases. 20 and 40 nm monomer radius ensemble  
 363 LDRs are also approaching this value at larger wavelengths.

364 LDR also increases with increasing number of monomers, although with  
365 a far less noticeable effect than monomer radius as shown in Figure 5a. A  
366 modification of the fractal dimension also induces small variations of the  
367 LDR, as presented in Figure 5b, lower fractal dimension inducing higher LDR  
368 values. This fractal dimension impact is amplified at larger monomer radius  
369 and smaller wavelength. At constant monomer radius, the LDR standard  
370 deviations overlap over the whole spectrum, for either different numbers of  
371 monomers or fractal dimensions.

## 372 5. Discussion

373 The monomer radius  $r_m$  appears to be the morphological parameter that  
374 influences the most the considered lidar-relevant radiative properties, as they  
375 all show large variations according to  $r_m$ . The monomer number has a strong  
376 impact on the lidar cross-sections ( $C_{back}$  and  $C_{ext}$ ), and a weak impact on  
377 lidar parameters (LR and LDR). The fractal dimension, although being an  
378 essential parameter of the fractal model, only induces low variations on the  
379 lidar-relevant radiative properties. In specific cases, as for the LR of small  
380 monomer radius aggregates presented on the blue curves of Figure 4b, it  
381 can present a significant impact. In order to stay faithful to realistic SFA  
382 morphologies, the variation range of the fractal dimension has been kept low.  
383 Hence, our results don't exclude the possibility that very high or very low  
384 fractal dimensions, *i.e.*  $D_f \approx 3$  or  $D_f \approx 1$ , might have larger impacts on  
385 these radiative properties.

386 The relatively strong dependence of the lidar cross-sections on the monomer  
387 radius and number seems to be related to the overall size of the aggre-  
388 gate, with larger geometrical cross-sections and volume of matter resulting  
389 in higher radiative cross-sections. In order to study this effect, we normal-  
390 ize the lidar cross-sections by  $(4/3)\pi N_m r_m^3$ , the volume occupied by a single  
391 aggregate, as in Equations (5) and (6). This effectively transforms these  
392 normalized cross-sections into the backscattering and extinction coefficients  
393 per soot volume fraction as shown in Equations (5) and (6). Results are  
394 presented in Figure 6.



(a) Volume normalized extinction cross-section variation with monomer radius and number (b) Volume normalized backscattering cross-section variation with monomer radius and number

Figure 6: Volume normalized cross-sections of SFA ensembles. The three sets of coloured curves are ordered according to the SFA ensemble monomer radius, *i.e.* 10 nm, 20 nm, and 40 nm monomer radius for the blue, red and green curves respectively. The full, dashed and dotted lines are associated with aggregates composed of 45, 125, and 450 monomers respectively. The error bars are plotted every four points and represent the standard deviations to the mean values of the volume normalized cross-sections. The fractal dimension is set to  $D_f = 1.8$  and the fractal prefactor of all aggregates is set to  $k_f = 1.3$ .

395 According to Figure 6, the monomer number dependence of both lidar  
 396 cross-sections is reduced by the normalization, but the monomer radius influence  
 397 is still observable, especially in the backscattering cross-sections. Indeed,  
 398 in the VIS to NIR part of the spectrum, increasing twofold the monomer  
 399 radius produces a slight increase of the volume normalized extinction cross-  
 400 section by 5 to 20% , while the volume normalized backscattering cross-  
 401 section is multiplied by a factor going from 1.5 up to 6. This indicates that  
 402 the link between backscattering and morphology in this spectrum can not  
 403 be fully described by the volume of matter of an aggregate. On the other  
 404 hand, the volume normalized extinction cross-section curves are much closer  
 405 together, indicating that extinction is more of a volume driven process. This  
 406 is also in agreement with the close extinction cross-sections values obtained  
 407 using volume equivalent spheres [20]. Taking Equations (5) and (6), this  
 408 implies that an increase of the soot volume fraction due to aggregates with  
 409 larger monomers would not produce the same effect on the extinction and  
 410 backscattering coefficients as an increase due to higher number of monomers.

411 The spectral dependence of the LDR is consistent with the fact that as  
412 the wavelength increases, the illuminating wave is less sensitive to the non-  
413 sphericity of the SFA. Indeed, as previously mentioned, spherical particles  
414 do not depolarize the scattered light in the backward direction. As the wave-  
415 length increases, the relative size of the aggregates compared to wavelength  
416 is smaller, and light is less sensitive to the shape irregularities. This is further  
417 supported by the low LDR of the  $r_m = 10$  nm SFA ensembles. The increasing  
418 LDR for lower fractal dimension, *i.e.* more linear SFAs, is consistent with  
419 the non-sphericity of an aggregate inducing more depolarization in the back-  
420 ward direction. The depolarization of soot fractal aggregate is a byproduct of  
421 the multiple scattering among primary particles [49], and is sensitive to the  
422 internal fine structure of the aggregates. By increasing the monomer radius,  
423 or equivalently reducing the wavelength, the LDR is increasingly sensitive to  
424 the fractal dimension. Still, these effects do not seem significant enough to  
425 estimate the fractal dimension using LDR measurements.

426 Even averaged over one hundred aggregates, the backscattering cross-  
427 section, LR and LDR standard deviations of ensembles of same morpho-  
428 logical parameters are important. The LDR and the LR being dependent  
429 on the backscattering cross section, these statistical deviations indicate that  
430 the backscattering cross section is sensitive to the fine structure of the ag-  
431 gregates. As the fractal parameters are nearly constant in each ensemble,  
432 it can be assumed that this morphological description is not sufficient in  
433 order to precisely describe an aggregate morphology and the resulting lidar-  
434 relevant radiative properties. Moreover, SFAs emitted from real combustion  
435 processes have been found to present observable differences from the fractal  
436 model used in this study. Indeed, the monomers can present overlapping,  
437 necking effect, or lognormal size distribution [50]. During their ageing, these  
438 particles can also be subject to morphology and composition changes, such  
439 as those induced by necking or coating phenomena [24, 51]. While these mor-  
440 phological properties can influence the radiative properties of soot aggregates  
441 [46, 52, 53], their impacts have not been investigated in this study, and SFAs  
442 are considered as composed of monodisperse spheres in point contact. The  
443 retrieval of soot morphological parameters through lidar measurements is a  
444 complex process, as the number of unknowns is potentially greater than the  
445 number of measurable quantities. Prior sensitivity studies would be required  
446 in order to describe in which magnitude a retrieval of soot morphological  
447 properties is possible, taking into account instrumental noise, polydispersion  
448 of any of the morphological parameters inside the measurement volume, and

449 range dependent quantities. Still, our results show promising outlooks for li-  
450 dar microphysical inversion, specifically for the retrieval of monomer radius.  
451 Knowledge of this morphological parameter could provide a first assessment  
452 of the LR values, likely allowing the use of an inverse algorithm in order to  
453 retrieve both backscattering and extinction coefficient profiles.

454 While the values of the computed lidar cross-sections and LDR are in  
455 good agreement with other modelled values found in the literature [46, 54],  
456 the LR values presented here are much higher than those usually used in lidar  
457 inversion methods [55]. Several factors can explain this discrepancy. As the  
458 interacting particles are part of a volume formed by the laser pulse divergence  
459 and length, soot can be mixed with other aerosols during lidar measurements,  
460 as in smoke. A second influencing factor could be the ageing status of the  
461 soot particles, as the atmospheric processing of these aerosols change their  
462 radiative properties. Considering the fractal model and the complex optical  
463 index dispersion law used in this study, our results are more relevant to  
464 freshly emitted SFAs, *i.e.* uncoated soot aerosols not yet influenced by ageing  
465 processes. Lidar measurements of freshly emitted soot particles would be of  
466 particular interest in order to compare our modelling results to experimental  
467 data, as, to our knowledge, there exist no such measurements in the literature.

## 468 6. Conclusion

469 This study aims at quantifying the radiative properties of Soot Fractal  
470 Aggregates that are most useful to process lidar measurements. Statistically  
471 representative ensembles of SFAs have been generated and results have been  
472 averaged over samples of one hundred aggregates of identical morphological  
473 parameters. In each ensemble, the morphology of any individual aggregate  
474 is still unique. This results in important standard deviations of the lidar-  
475 relevant radiative properties and supports the need for statistically represen-  
476 tative ensembles. It also suggests that the fractal model is not self-sufficient  
477 in order to describe the morphology of fractal aggregates, and that other mor-  
478 phological parameters might be needed. Our objectives was also to quantify  
479 realistic wavelength dependence of the aggregate radiative properties. This  
480 was achieved by computing them over a wide spectrum and by considering a  
481 realistic wavelength dependent refractive index, although other values exist  
482 in the literature.

483 The main conclusions of this study are :

- 484 - The monomer radius  $r_m$  strongly influences all of the studied lidar-  
485 relevant radiative properties.
- 486 - The number of monomers per aggregate  $N_m$  has also a strong effect on  
487 the lidar cross-sections, but has a limited impact on the lidar paramete-  
488 ters such as the Lidar Ratio and the linear depolarization ratio.
- 489 - The aggregate fractal dimension  $D_f$  has a weak impact on all lidar-  
490 relevant radiative properties.

491 These results are quite significant for lidar application, as the processing  
492 of the elastic lidar products (*i.e.* backscattering coefficients  $\beta$ , extinction  
493 coefficients  $\alpha$  and volume depolarization ratio  $\delta_v$ ) might provide means to  
494 evaluate the monomer radius.

## 495 7. Acknowledgements

496 This work has been partially funded by the doctoral school Sciences  
497 mécaniques et énergétiques, matériaux et géosciences (SMEMAG) and the  
498 ONERA, and was conducted in the framework of the PROMETE project.  
499 We would like to acknowledge Daniel W. Mackowski for making publicly  
500 available the MSTM code, as well as Matthew J. Berg and Christopher M.  
501 Sorensen.

## 502 8. References

- 503 [1] S. Forrest, T. Witten Jr, Long-range correlations in smoke-particle ag-  
504 gregates, *Journal of Physics A: Mathematical and General* 12 (1979)  
505 L109.
- 506 [2] Ü. Ö. Köylü, G. Faeth, T. L. Farias, M. d. G. Carvalho, Fractal and pro-  
507 jected structure properties of soot aggregates, *Combustion and Flame*  
508 100 (1995) 621–633.
- 509 [3] E. J. Highwood, R. P. Kinnersley, When smoke gets in our eyes: The  
510 multiple impacts of atmospheric black carbon on climate, air quality  
511 and health, *Environment International* 32 (2006) 560–566.
- 512 [4] B. Kärcher, Formation and radiative forcing of contrail cirrus, *Nature*  
513 *communications* 9 (2018) 1824.

- 514 [5] O. Boucher, D. Randall, P. Artaxo, C. Bretherton, G. Feingold,  
515 P. Forster, V.-M. Kerminen, Y. Kondo, H. Liao, U. Lohmann, P. Rasch,  
516 S. Satheesh, S. Sherwood, B. Stevens, X. Zhang, *Clouds and Aerosols*,  
517 Cambridge University Press, Cambridge, United Kingdom and New  
518 York, NY, USA, p. 571–658.
- 519 [6] G. Myhre, D. Shindell, F.-M. Bréon, W. Collins, J. Fuglestvedt,  
520 J. Huang, D. Koch, J.-F. Lamarque, D. Lee, B. Mendoza, T. Naka-  
521 jima, A. Robock, G. Stephens, T. Takemura, H. Zhang, *Anthropogenic*  
522 *and Natural Radiative Forcing*, Cambridge University Press, Cambridge,  
523 United Kingdom and New York, NY, USA, p. 659–740.
- 524 [7] R. K. Chakrabarty, N. D. Beres, H. Moosmüller, S. China, C. Mazzoleni,  
525 M. K. Dubey, L. Liu, M. I. Mishchenko, Soot superaggregates from  
526 flaming wildfires and their direct radiative forcing, *Scientific reports* 4  
527 (2014) 5508.
- 528 [8] L. Tumolva, J.-Y. Park, J.-s. Kim, A. L. Miller, J. C. Chow, J. G. Wat-  
529 son, K. Park, Morphological and elemental classification of freshly emit-  
530 ted soot particles and atmospheric ultrafine particles using the tem/eds,  
531 *Aerosol Science and Technology* 44 (2010) 202–215.
- 532 [9] G. Okyay, E. Héripré, T. Reiss, P. Haghi-Ashtiani, T. Auger, F. Engue-  
533 hard, Soot aggregate complex morphology: 3d geometry reconstruction  
534 by sem tomography applied on soot issued from propane combustion,  
535 *Journal of Aerosol Science* 93 (2016) 63–79.
- 536 [10] F.-X. Ouf, P. Parent, C. Laffon, I. Marhaba, D. Ferry, B. Marcillaud,  
537 E. Antonsson, S. Benkoula, X.-J. Liu, C. Nicolas, et al., First in-flight  
538 synchrotron x-ray absorption and photoemission study of carbon soot  
539 nanoparticles, *Scientific reports* 6 (2016) 36495.
- 540 [11] J. D. Black, M. P. Johnson, In-situ laser-induced incandescence of soot  
541 in an aero-engine exhaust: Comparison with certification style measure-  
542 ments, *Aerospace Science and Technology* 14 (2010) 329–337.
- 543 [12] H. Michelsen, C. Schulz, G. Smallwood, S. Will, Laser-induced incan-  
544 descence: Particulate diagnostics for combustion, atmospheric, and in-  
545 dustrial applications, *Progress in Energy and Combustion Science* 51  
546 (2015) 2–48.



- 547 [13] M. Bouvier, J. Yon, G. Lefevre, F. Grisch, A novel approach for in-situ  
548 soot size distribution measurement based on spectrally resolved light  
549 scattering, *Journal of Quantitative Spectroscopy and Radiative Transfer*  
550 225 (2019) 58–68.
- 551 [14] D. Müller, F. Wagner, U. Wandinger, A. Ansmann, M. Wendisch, D. Al-  
552 thausen, W. von Hoyningen-Huene, Microphysical particle parameters  
553 from extinction and backscatter lidar data by inversion with regulariza-  
554 tion: experiment, *Applied Optics* 39 (2000) 1879–1892.
- 555 [15] A. Miffre, G. David, B. Thomas, P. Rairoux, Atmospheric non-spherical  
556 particles optical properties from uv-polarization lidar and scattering ma-  
557 trix, *Geophysical Research Letters* 38 (2011).
- 558 [16] A. H. Omar, D. M. Winker, M. A. Vaughan, Y. Hu, C. R. Trepte, R. A.  
559 Ferrare, K.-P. Lee, C. A. Hostetler, C. Kittaka, R. R. Rogers, et al.,  
560 The calipso automated aerosol classification and lidar ratio selection  
561 algorithm, *Journal of Atmospheric and Oceanic Technology* 26 (2009)  
562 1994–2014.
- 563 [17] S. Burton, R. Ferrare, C. Hostetler, J. Hair, R. Rogers, M. Obland,  
564 C. Butler, A. Cook, D. Harper, K. Froyd, Aerosol classification using  
565 airborne high spectral resolution lidar measurements—methodology and  
566 examples, *Atmospheric Measurement Techniques* 5 (2012) 73–98.
- 567 [18] J. D. Klett, Lidar inversion with variable backscatter/extinction ratios,  
568 *Applied optics* 24 (1985) 1638–1643.
- 569 [19] D. Mackowski, M. Mishchenko, A multiple sphere t-matrix fortran code  
570 for use on parallel computer clusters, *Journal of Quantitative Spec-  
571 troscopy and Radiative Transfer* 112 (2011) 2182–2192.
- 572 [20] R. Ceolato, F. Gaudfrin, O. Pujol, N. Riviere, M. J. Berg, C. M.  
573 Sorensen, Lidar cross-sections of soot fractal aggregates: Assessment  
574 of equivalent-sphere models, *Journal of Quantitative Spectroscopy and  
575 Radiative Transfer* 212 (2018) 39–44.
- 576 [21] M. Mishchenko, J. Hovenier, Depolarization of light backscattered by  
577 randomly oriented nonspherical particles., *Optics Letters* 20 (1995)  
578 1356–1358.

- 579 [22] M. I. Mishchenko, *Electromagnetic scattering by particles and particle*  
580 *groups: an introduction*, Cambridge University Press, 2014.
- 581 [23] P. Buseck, K. Adachi, A. Gelencsér, É. Tompa, M. Pósfai, *Are black*  
582 *carbon and soot the same?*, *Atmospheric Chemistry and Physics Dis-*  
583 *cussions* 12 (2012) 24821–24846.
- 584 [24] W. R. Heinson, P. Liu, R. K. Chakrabarty, *Fractal scaling of coated*  
585 *soot aggregates*, *Aerosol Science and Technology* 51 (2017) 12–19.
- 586 [25] C. M. Sorensen, G. C. Roberts, *The prefactor of fractal aggregates*,  
587 *Journal of colloid and interface science* 186 (1997) 447–452.
- 588 [26] Ü. Ö. Köylü, G. M. Faeth, *Structure of overfire soot in buoyant turbulent*  
589 *diffusion flames at long residence times*, *Combustion and Flame* 89  
590 (1992) 140–156.
- 591 [27] T. C. Bond, R. W. Bergstrom, *Light absorption by carbonaceous parti-*  
592 *cles: An investigative review*, *Aerosol science and technology* 40 (2006)  
593 27–67.
- 594 [28] G. Mulholland, W. Liggett, H. Koseki, *The effect of pool diameter on*  
595 *the properties of smoke produced by crude oil fires*, in: *Symposium*  
596 *(International) on Combustion*, volume 26, Elsevier, pp. 1445–1452.
- 597 [29] K. A. Jensen, J. M. Suo-Anttila, L. G. Blevins, *Measurement of soot*  
598 *morphology, chemistry, and optical properties in the visible and near-*  
599 *infrared spectrum in the flame zone and overfire region of large jp-8 pool*  
600 *fires*, *Combustion Science and Technology* 179 (2007) 2453–2487.
- 601 [30] M. Lapuerta, J. Barba, A. D. Sediako, M. R. Kholghy, M. J. Thomson,  
602 *Morphological analysis of soot agglomerates from biodiesel surrogates*  
603 *in a coflow burner*, *Journal of Aerosol Science* 111 (2017) 65–74.
- 604 [31] C. Sorensen, *The mobility of fractal aggregates: a review*, *Aerosol*  
605 *Science and Technology* 45 (2011) 765–779.
- 606 [32] D. W. Mackowski, *Electrostatics analysis of radiative absorption by*  
607 *sphere clusters in the rayleigh limit: application to soot particles*, *Ap-*  
608 *plied optics* 34 (1995) 3535–3545.

- 609 [33] D. W. Mackowski, A simplified model to predict the effects of aggrega-  
610 tion on the absorption properties of soot particles, *Journal of Quanti-*  
611 *tative Spectroscopy and Radiative Transfer* 100 (2006) 237–249.
- 612 [34] F. Liu, G. J. Smallwood, Radiative properties of numerically gener-  
613 ated fractal soot aggregates: the importance of configuration averaging,  
614 *Journal of heat transfer* 132 (2010) 023308.
- 615 [35] Ü. Ö. Köylü, G. Faeth, Spectral extinction coefficients of soot aggregates  
616 from turbulent diffusion flames, *Journal of Heat Transfer* 118 (1996)  
617 415–421.
- 618 [36] M. Schnaiter, H. Horvath, O. Möhler, K.-H. Naumann, H. Saathoff,  
619 O. Schöck, Uv-vis-nir spectral optical properties of soot and soot-  
620 containing aerosols, *Journal of Aerosol Science* 34 (2003) 1421–1444.
- 621 [37] J. Yon, A. Bescond, F. Liu, On the radiative properties of soot aggre-  
622 gates part 1: Necking and overlapping, *Journal of Quantitative Spec-*  
623 *troscopy and Radiative Transfer* 162 (2015) 197–206.
- 624 [38] H.-C. Chang, T. Charalampopoulos, Determination of the wavelength  
625 dependence of refractive indices of flame soot, *Proc. R. Soc. Lond. A*  
626 430 (1990) 577–591.
- 627 [39] T. Nishizawa, N. Sugimoto, I. Matsui, A. Shimizu, B. Tatarov,  
628 H. Okamoto, Algorithm to retrieve aerosol optical properties from high-  
629 spectral-resolution lidar and polarization mie-scattering lidar measure-  
630 ments, *IEEE Transactions on Geoscience and Remote Sensing* 46 (2008)  
631 4094–4103.
- 632 [40] H. Li, C. Liu, L. Bi, P. Yang, G. W. Kattawar, Numerical accuracy of  
633 “equivalent” spherical approximations for computing ensemble-averaged  
634 scattering properties of fractal soot aggregates, *Journal of Quantitative*  
635 *Spectroscopy and Radiative Transfer* 111 (2010) 2127–2132.
- 636 [41] C. Sorensen, Light scattering by fractal aggregates: a review, *Aerosol*  
637 *Science & Technology* 35 (2001) 648–687.
- 638 [42] Y. Zhao, L. Ma, Applicable range of the rayleigh-debye-gans theory for  
639 calculating the scattering matrix of soot aggregates, *Applied optics* 48  
640 (2009) 591–597.

- 641 [43] J. Dong, J. Zhao, L. Liu, Morphological effects on the radiative prop-  
642 erties of soot aerosols in different internally mixing states with sulfate,  
643 *Journal of Quantitative Spectroscopy and Radiative Transfer* 165 (2015)  
644 43–55.
- 645 [44] F. Liu, J. Yon, A. Bescond, On the radiative properties of soot  
646 aggregates–part 2: Effects of coating, *Journal of Quantitative Spec-*  
647 *troscopy and Radiative Transfer* 172 (2016) 134–145.
- 648 [45] K. Adachi, S. H. Chung, P. R. Buseck, Shapes of soot aerosol particles  
649 and implications for their effects on climate, *Journal of Geophysical*  
650 *Research: Atmospheres* 115 (2010).
- 651 [46] M. I. Mishchenko, L. Liu, D. W. Mackowski, T-matrix modeling of lin-  
652 ear depolarization by morphologically complex soot and soot-containing  
653 aerosols, *Journal of Quantitative Spectroscopy and Radiative Transfer*  
654 123 (2013) 135–144.
- 655 [47] Y. Wu, T. Cheng, L. Zheng, H. Chen, Effect of morphology on the  
656 optical properties of soot aggregated with spheroidal monomers, *Journal*  
657 *of Quantitative Spectroscopy and Radiative Transfer* 168 (2016) 158–  
658 169.
- 659 [48] D. W. Mackowski, M. I. Mishchenko, Calculation of the t matrix and  
660 the scattering matrix for ensembles of spheres, *JOSA A* 13 (1996) 2266–  
661 2278.
- 662 [49] N. Lu, C. Sorensen, Depolarized light scattering from fractal soot ag-  
663 gregates, *Physical Review E* 50 (1994) 3109.
- 664 [50] A. Bescond, J. Yon, F. Ouf, D. Ferry, D. Delhayé, D. Gaffié, A. Coppalle,  
665 C. Rozé, Automated determination of aggregate primary particle size  
666 distribution by tem image analysis: application to soot, *Aerosol Science*  
667 *and Technology* 48 (2014) 831–841.
- 668 [51] X. Ma, C. D. Zangmeister, J. Gigault, G. W. Mulholland, M. R.  
669 Zachariah, Soot aggregate restructuring during water processing, *Journal*  
670 *of Aerosol Science* 66 (2013) 209–219.

- 671 [52] J. Luo, Y. Zhang, Q. Zhang, F. Wang, J. Liu, J. Wang, Sensitivity  
672 analysis of morphology on radiative properties of soot aerosols, *Optics*  
673 *express* 26 (2018) A420–A432.
- 674 [53] J. Yin, L. Liu, Influence of complex component and particle polydis-  
675 persity on radiative properties of soot aggregate in atmosphere, *Journal*  
676 *of Quantitative Spectroscopy and Radiative Transfer* 111 (2010) 2115–  
677 2126.
- 678 [54] N. Doner, F. Liu, Impact of morphology on the radiative properties  
679 of fractal soot aggregates, *Journal of Quantitative Spectroscopy and*  
680 *Radiative Transfer* 187 (2017) 10–19.
- 681 [55] A. J. Illingworth, H. Barker, A. Beljaars, M. Ceccaldi, H. Chepfer,  
682 N. Clerbaux, J. Cole, J. Delanoë, C. Domenech, D. P. Donovan, et al.,  
683 The earthcare satellite: The next step forward in global measurements of  
684 clouds, aerosols, precipitation, and radiation, *Bulletin of the American*  
685 *Meteorological Society* 96 (2015) 1311–1332.